

Madden-Julian oscillation winds excite an intraseasonal see-saw of ocean mass that affects Earth's polar motion

M. Afroosa^{1,2,8}, B. Rohith^{1,8} , Arya Paul¹  , Fabien Durand^{3,4}, Romain Bourdallé-Badie⁵, P. V. Sreedevi^{1,6} , Olivier de Viron⁷, Valérie Ballu⁷  & S. S. C. Shenoi¹

Strong large-scale winds can relay their energy to the ocean bottom and elicit an almost immediate intraseasonal barotropic (depth independent) response in the ocean. The intense winds associated with the Madden-Julian Oscillation over the Maritime Continent generate significant intraseasonal basin-wide barotropic sea level variability in the tropical Indian Ocean. Here we show, using a numerical model and a network of in-situ bottom pressure recorders, that the concerted barotropic response of the Indian and the Pacific Ocean to these winds leads to an intraseasonal see-saw of oceanic mass in the Indo-Pacific basin. This global-scale mass shift is unexpectedly fast, as we show that the mass field of the entire Indo-Pacific basin is dynamically adjusted to Madden-Julian Oscillation in a few days. We find this large-scale ocean see-saw, induced by the Madden-Julian Oscillation, has a detectable influence on the Earth's polar axis motion, in particular during the strong see-saw of early 2013.

¹Indian National Centre for Ocean Information Services (INCOIS), Ministry of Earth Science (MoES), Hyderabad, India. ²School of Ocean Sciences & Technology, Kerala University of Fisheries and Ocean Studies (KUFOS), Cochin, India. ³LEGOS, Université de Toulouse, IRD, CNRS, CNES, UPS, Toulouse, France. ⁴Laboratório de Geoquímica, Instituto de Geociências, Universidade de Brasília, Brasília, Brazil. ⁵Mercator Ocean International, Ramonville, France. ⁶Cochin University of Science and Technology, Cochin, India. ⁷LIENSs, La Rochelle, France. ⁸These authors contributed equally: M. Afroosa, B. Rohith. ✉email: aryapaul@incois.gov.in

The Madden–Julian oscillation (MJO) is the most energetic large-scale intraseasonal atmospheric disturbance^{1,2}. It originates in tropical Africa and travels eastward through the Indian and the Pacific basins as 1st and 2nd zonal wave-numbers of zonal wind, precipitation, and convection³. Eventually, these disturbances die out over the Atlantic Ocean and the African Continent. These disturbances are largely confined in the tropical belt. Strong boreal winter MJO is associated with intense winds over the Maritime Continent, the tropical interface between the Indian and the Pacific Ocean, generating significant intraseasonal barotropic sea-level variability in the entire tropical Indian Ocean⁴. It amounts to a basin-scale signal that reaches up to 4–6 cm in the tropical Indian Ocean, with the mass redistribution achieved through fast-propagating barotropic waves adjusting the tropical Indian Ocean in ~2–3 days⁴. Past studies on the impact of MJO on the global ocean barotropic variability have been rare⁵. We report that during boreal winter MJO, the rise of oceanic mass in the tropical Indian Ocean is concurrent with a fall of oceanic mass in the Pacific Ocean, and vice versa at intraseasonal timescales. The periodic reversal of MJO winds, therefore, leads to an intraseasonal see-saw in the oceanic mass in the Indo–Pacific basin, with the fulcrum stationed over the Maritime Continent. Due to the extent of the Pacific Ocean—well beyond the tropics—this fast barotropic dynamics incites a far-reaching, quasi-global oceanic response to the MJO encompassing tens of thousands of kilometers within a few days. This challenges the earlier understanding of response only via slow-propagating baroclinic waves thereby adjusting the density field of the basins in ~2–3 months^{6,7}.

The Earth's rotation about its three axes is not constant, and presents fluctuations over a broad range of frequencies^{8–13}. The rotation changes are classically separated into two parts: the changes in the angular velocity are described in terms of changes in the length-of-day, whereas the rotation of the solid Earth around its rotation axis corresponds to polar motion^{11–13}. Most of those signals come from the exchange of angular momentum between the solid Earth and the fluid parts, namely the Earth's core and its fluid envelope (atmosphere and ocean)^{11,13,14}. For geometry reasons, the atmosphere impacts dominate that from the ocean for the length-of-day, except at tidal frequencies¹⁴. The picture is more complex for polar motion, for which the relative domination of the ocean or atmosphere depends on the frequency band. In the intraseasonal band of interest for our study, the polar motion is mostly forced by the atmosphere⁸. However, the contribution from the ocean is also significant^{8,15,16}. The impact from the ocean on polar motion mostly comes from the spatial distribution of the oceanic mass, though, for some particular phenomena, the mass transport gives rise to an observable change^{8,15,16}. The see-saw generation involves large-scale mass redistribution and currents across and within the Pacific and the Indian basins. The associated global-scale angular momentum, arising both from a large-scale circulation in the ocean and a global-scale mass redistribution, is expected to leave its signature in the Earth's rotation about its polar axis and the polar motion^{8–10,13}. Our study demonstrates that the MJO-induced see-saw, being a large-scale process, does leave oceanic footprints on the polar motion. The excitations induced by the oceans, though generally minor, are at times up to about half the magnitude as those induced by the atmosphere.

Results and discussion

Revelation of the see-saw. The see-saw is evidenced through a high-resolution global ocean circulation model, Nucleus for European Modelling of the Ocean (NEMO)¹⁷, which can resolve adequately the narrow Indonesian straits between the Indian and

the Pacific basins. The control run (see methods section) covers the 2009–2019 period and captures fairly well the Indonesian Throughflow transports (Supplementary Fig. 1) and the observed ocean mass variability at intraseasonal timescales (Supplementary Fig. 2). This whole study focuses on intraseasonal timescales (30–80 days band) during boreal winter (December–April) months. All quantities subsequently analyzed have been intraseasonally filtered using Lanczos filter to isolate the 30–80 days timescale unless otherwise mentioned. We define a See-saw Index from the control run as the normalized difference of mean equivalent water depth between the Indian and the Pacific basins. A positive index indicates a high water level in the Indian Ocean and a low water level in the Pacific Ocean. In Fig. 1a, the time series of the See-saw Index (shaded gray) and the net volume flux into the Indian (red line) and the Pacific (blue line) Ocean are plotted for the period 2009–2019. The See-saw Index variability is strongest during 2011–2012 and 2012–2013—two winters of strong MJO activity (Fig. 1c) over the Maritime Continent. Most of the time, and in particular during intense MJO events, the two-volume fluxes are in opposite phase, i.e., a net inflow of water in the Indian Ocean is accompanied by a net outflow of water from the Pacific Ocean and vice versa, thereby displaying characteristics of a see-saw in the Indo–Pacific basin. As expected, the maximum transports occur at the times of sign change of the See-saw Index (Fig. 1b). During a strong positive See-saw Index peak, ~1.5 Sv [$1 \text{ Sv} = 10^6 \text{ m}^3 \text{ s}^{-1}$] of water is gained by the Indian Ocean, whereas ~2.6 Sv of water is lost by the Pacific Ocean. This is equivalent to a spatially uniform basin rise of ~1.0 cm in the Indian Ocean and a concurrent fall of ~0.8 cm of equivalent water depth in the Pacific Ocean. The Southern Ocean closes the volume budget. These dynamics reverse during the negative peak of the See-saw Index (Supplementary Fig. 3).

To explore the spatial extent of this see-saw, the anomaly in equivalent water depth over the Maritime Continent (at the location of the yellow star on Fig. 2a) is correlated with the anomaly in equivalent water depth at all model grid locations during December–April. Only those correlations that exceed 90% significance (see methods section) are shown. Interestingly, a basin-wide rise in equivalent water depth in the tropical Indian Ocean is accompanied by a large-scale fall in equivalent water depth extending over the tropics, the southern extratropics and the northern edge of the Pacific Ocean and over most parts of the Arctic Ocean (Fig. 2a). In contrast, only isolated small patches in the Atlantic Ocean participating in this coherent dance of oceanic mass. It is striking to discover that a large-scale see-saw of oceanic mass encompasses the Indo–Pacific basin and extends further over the vast majority of the world ocean.

Role of MJO. The large-scale anomaly in equivalent water depth variability in the tropical Indian Ocean is driven by MJO winds over the Maritime Continent⁴. To determine to which extent the MJO winds also drive the large-scale variability in the Pacific Ocean, a sensitivity model experiment (MC-EXP; see methods section) is run for the 2009–2019 period, with wind forcing restricted to the Maritime Continent (black box in Fig. 2b). The spatial correlation of anomaly in equivalent water depth over the Maritime Continent from MC-EXP during each December–April with the same at all model grid points is plotted in Fig. 2b. The correlation pattern in the Indo–Pacific basin is, to a large extent, similar to the correlation pattern obtained from the control run (Fig. 2a). So, the intraseasonal see-saw in the Indo–Pacific basin persists even if the model is forced only by winds over the Maritime Continent. Note that the signature is not consistent with what is observed in the anomaly in equivalent water depth in

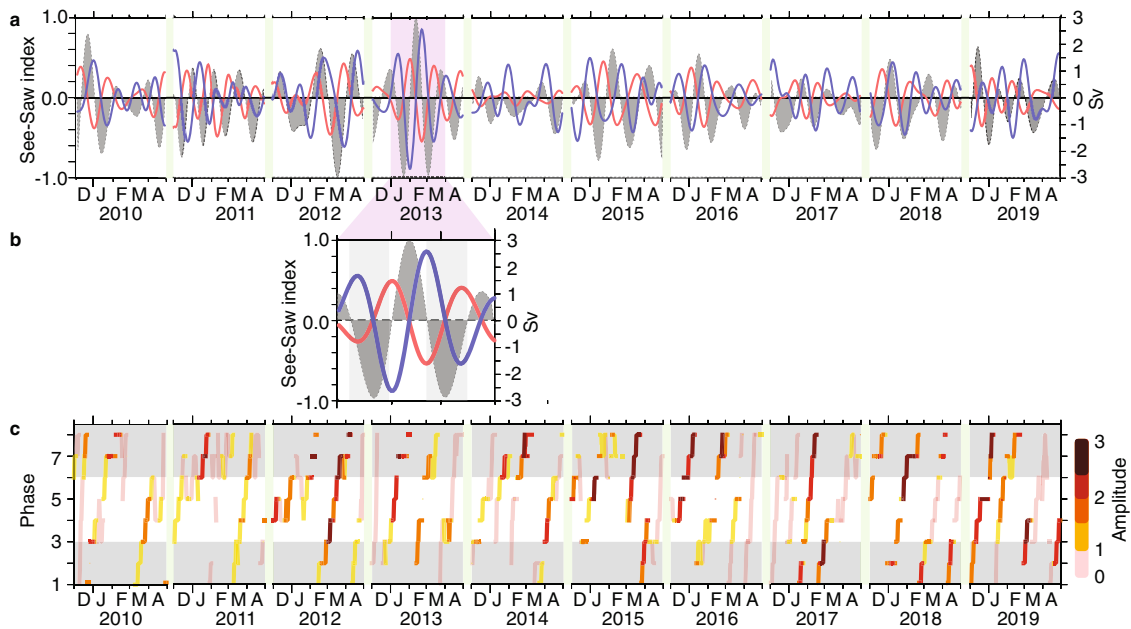


Fig. 1 Transports in the Indo-Pacific basin and MJO index time series. **a** Time series of the See-saw Index (shaded gray) and the net intraseasonal flux (in Sv) in the Indian (red line) and the Pacific (blue line) basin during each December–April of 2009–2019 estimated from the control run. **b** Inset of **a** for one strong see-saw event in early 2013. **c** Amplitude and phase of MJO index⁵⁹ during 2009–2019. MJO is over the Maritime Continent when it is in between phases 3 and 6 (unshaded band).

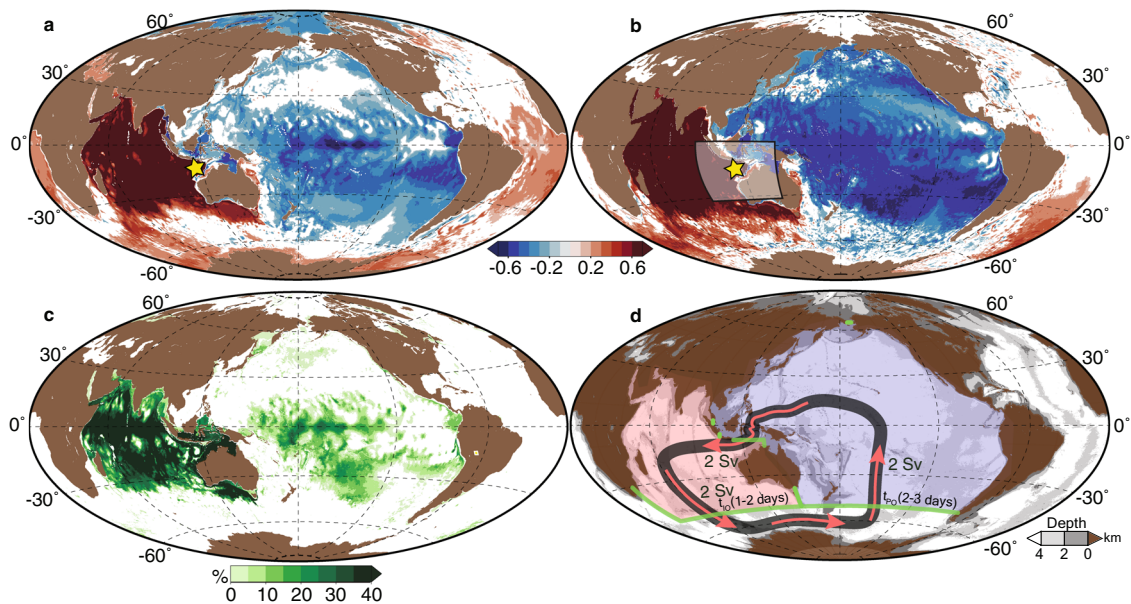


Fig. 2 See-saw pattern and associated circulation. The plot of correlation (>90% significance; see methods section) of intraseasonal equivalent water depth over the Maritime Continent at 117.94°E, 15.02°S (yellow star) with respect to the intraseasonal equivalent water depth at all grid locations derived from **a** control run and **b** MC-EXP. **c** The percentage of intraseasonal equivalent water depth variance in the control run explained by MC-EXP. The black box in **b** represents the extent of wind forcing in MC-EXP. The variance captured is calculated using the equation, $1 - \frac{\text{variance}(A-B)}{\text{variance}(A)}$, where A represents the control run and B denotes MC-EXP. **d** The schematic illustration of the intraseasonal barotropic circulation during a positive cycle of a see-saw event. The red (blue) tinge in the Indian (Pacific) Ocean represents a basin-wide rise (fall) in intraseasonal equivalent water depth. The green lines define the boundaries of the Indian and the Pacific basins across which volume fluxes are estimated in **a** and **b**. The mean intraseasonal equivalent water depth difference between the area covered by red and the blue tinge in the Indian and the Pacific basin is used to define the See-saw Index. t_{IO} and t_{PO} represent the delay in the intraseasonal transport with respect to the intraseasonal transport across the Indonesian straits. Gray shades represent the bathymetry.

the Arctic and the North Pacific Ocean, most probably due to dominant local dynamics^{18,19}.

Whereas the MC-EXP largely captures the variance in the tropical Indian Ocean (with values >70%)⁴, its impact is also significant over the Pacific Ocean (Fig. 2c). The winds over the

Maritime Continent alone can generate as much as ~15–20% of variance in the equivalent water depth over the tropical and the southern Pacific Ocean. The rest of the variability in the Pacific Ocean may be an outcome of local dynamics and/or remote effects that owe their origin outside the Maritime Continent. In

contrast, the Arctic and the Atlantic Ocean are mostly not influenced by the winds over the Maritime Continent. Nevertheless, it is remarkable that the wind forcing from such a small region (~4% of global ocean coverage) casts such a large-scale influence and excites ~15–20% of the intraseasonal oceanic mass fluctuations over a large part of the tropical Pacific.

During a positive cycle of the index, the MJO winds drive ~2 Sv of Pacific waters into the Indian Ocean through the Indonesian straits. An equivalent flux is subsequently flushed out into the Southern Ocean after ~1–2 days. The Southern Ocean conveys it eastward and subsequently injects ~2 Sv into the Pacific Ocean after another ~1 day, thereby closing this anticlockwise circulation around the Australian continent (Supplementary Fig. 4). This barotropic circulation is schematically illustrated in Fig. 2d. As expected, the circulation reverses its direction during the negative phase of the see-saw. This intraseasonal circulation occurs over and above a permanent anticlockwise barotropic circulation around the Australian continent²⁰. It is this intraseasonal reversing circulation that drives the Indo–Pacific see-saw.

Observational imprint of the see-saw. We investigated the imprint of the intraseasonal see-saw through the bottom pressure recorder network, although this network is very sparse. Figure 3a shows the evolution of intraseasonal equivalent water depth from two bottom pressure recorders, one located in the Maritime Continent (BPR-MC; red line) and another one in the central Pacific Ocean (BPR-PAC; blue line) during boreal winters of 2009–2019 (see methods section for data processing). BPR-PAC is often out-of-phase with BPR-MC, particularly in 2011–2012 and 2012–2013, when the MJO wind stress was strong over the Maritime Continent. The variability in the BPR-MC amounts to 4–6 cm peak-to-peak, that of the BPR-PAC is ~2–3 cm—half compared to the Indian Ocean. Anomaly in equivalent water depth at the BPR-MC was correlated with anomaly in equivalent water depth from all available bottom pressure recorders globally and all bottom pressure recorders whose significance (see

methods section) exceeds 90% are plotted in Fig. 3b. Nineteen out of forty-five (~42%) bottom pressure recorders in the Pacific Ocean exhibit a significant correlation. All the Indian Ocean bottom pressure recorders synchronously oscillate, whereas all the bottom pressure recorders in the Pacific and in the Arctic Ocean are anticorrelated with the bottom pressure recorders in the Indian Ocean. The observed features are in line with the model results, and consistent with what is expected from the existence of a large-scale see-saw between the Indian and the Pacific basins.

See-saw impact on polar motions. The geometry of the see-saw circulation (Fig. 2d) is near-optimal for generating a large signature in the polar motion excitation. The excitation of the polar motion is classically estimated using excitation functions— χ_1 for rotation around an axis at the Greenwich meridian (x axis) and χ_2 for rotation around an axis that passes through the Indian Ocean at 90°E (y axis) (see methods section). Considering the geometry of the currents shown in Fig. 2d, the see-saw motion mostly impacts the polar motion through χ_2 . Due to the Chandler wobble resonance that dominates the polar motion^{21,22}, it is not possible to directly compare our model-derived estimates with the polar motion observation. However, we can compute the excitation functions required to generate the observed polar motion during the strong see-saw of 2012–2013.

Detection of 2012–2013 event. The ocean is the only one of the contributors to intraseasonal polar motion excitation—the atmosphere and the hydrology being the other sources^{8,15}. An oceanic signal can only be separated from the climate noise if it is sensibly larger in the excitation than the nonoceanic contributions, or if we can correct the observed excitation with such precision that the residuals are notably smaller than the oceanic contribution. When dealing with intraseasonal excitation, the standard deviation, estimated over the last 10 years, is at the level of ~16 milliarcseconds (mas), to be compared with the 40 mas of the MJO-induced ocean signature, which makes it necessary to

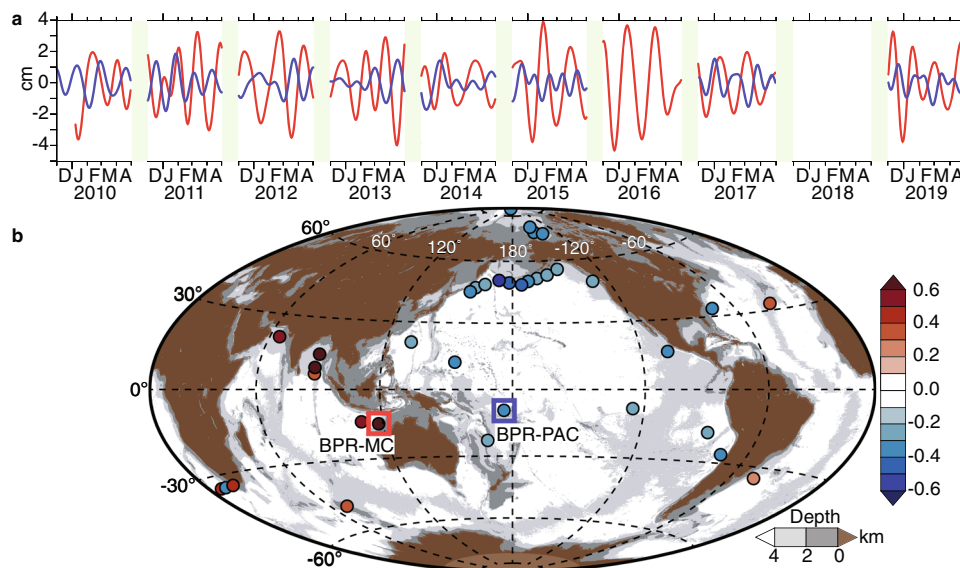


Fig. 3 See-saw in the bottom pressure recorders. **a** The plot of intraseasonal equivalent water depth at the BPR-MC (solid red; 117.94°E, 15.02°S, 5664 m) and the BPR-PAC (solid blue; 176.32°E, 9.517°S, 4921 m) during each December–April from 2009 to 2019. **b** Correlation (>90% significance; see methods section) of intraseasonal equivalent water depth from bottom pressure recorders across the globe with respect to the intraseasonal equivalent water depth at the BPR-MC (red box). All other bottom pressure recorders are marked as solid circles. The blue square box is used to mark BPR-PAC. The background color shades represent the bathymetry. The number of bottom pressure recorders analyzed in the Indian Ocean, Pacific Ocean, Atlantic Ocean, and the Arctic Ocean are 8, 45, 23, and 6, respectively.

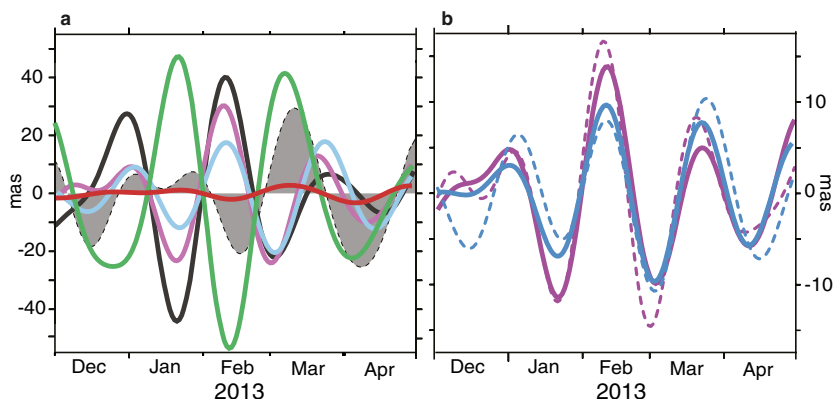


Fig. 4 Ocean signature in polar motion. **a** The plot of the time evolution of intraseasonal χ_2 from International Earth Rotation and Reference Systems Service (IERS) observations (gray shaded), atmospheric angular momentum (green), and hydrological angular momentum (red) from ESMGFZ, residual of IERS observation after removing atmospheric and hydrological angular momentum from ESMGFZ (black), χ_2 from control run (violet) and MC-EXP (cyan) during 2012–2013 boreal winter. **b** The plot of the time evolution of mass (dotted lines) and motion (solid lines) component of oceanic contribution to intraseasonal χ_2 from control run (violet) and MC-EXP (cyan) during 2012–2013 boreal winter. Note the difference in scales in **a** and **b**.

subtract the nonoceanic signal. The raw observed excitation (shaded gray) during 2012–2013 is plotted in Fig. 4a, together with the residuals (solid black) when the nonoceanic signals are subtracted. The contributions from the atmosphere (solid green) and hydrology (solid red), estimated from the Earth System Model ESMGFZ^{23–27}, are also plotted to analyze the relative contributions of ocean, atmosphere, and hydrology. The most dominant contribution to the intraseasonal polar motion comes from the atmosphere as expected^{8,10}. We also observe a strong oceanic signal in early 2013. The oceanic contribution is of comparable order of magnitude as the atmosphere, whereas the contribution from hydrology is relatively negligible. The oceanic signal is primarily out of phase with the atmospheric signal and hence subdues the intraseasonal polar motion excitations caused by the atmosphere. The ocean, therefore, dampens the intraseasonal polar motion excitations caused by the atmosphere.

How much of this oceanic signal owes its origin to the MJO winds over the Maritime Continent during 2012–2013? During weak MJO years, the oceanic excitation of polar motion is not significantly influenced by the barotropic processes originating in the Maritime Continent (Supplementary Fig. 5). In contrast, during the 2012–2013 strong MJO event, the ocean angular momentum from the MC-EXP (Fig. 4a; cyan curve) captures ~70% of the variance of the oceanic signal from the control run. In addition, MC-EXP is in phase with the residual geodetic excitation function (Fig. 4a; black curve) and the oceanic excitation computed from the MC-EXP captures ~50% of the variance of the residual geodetic excitation. This is surprising because the MC-EXP captures ~15–20% of the variance of equivalent water depth in some regions of the Pacific Ocean, and 70% in the Indian Ocean from the control run. This is possible because the mass and motion terms of the ocean excitation estimated from the MC-EXP are similar in magnitude (Fig. 4b), which stands in stark contrast with earlier findings that suggested the mass term dominates the motion term by a factor of 5–10 over a broad range of frequencies, including the intraseasonal timescales¹⁰. The ocean mass and ocean motion terms are synchronous and thereby constructively add up during 2012–2013 to yield a detectable signal up to about half the magnitude as its atmospheric counterpart. This synchronicity of mass and motion term is relatively weak or absent during other years (Supplementary Fig. 6)—particularly during weak MJO years—leading to subdued oceanic excitations during see-saw events. Nevertheless, the agreement in amplitude and phase between the residual excitation and the ocean excitation

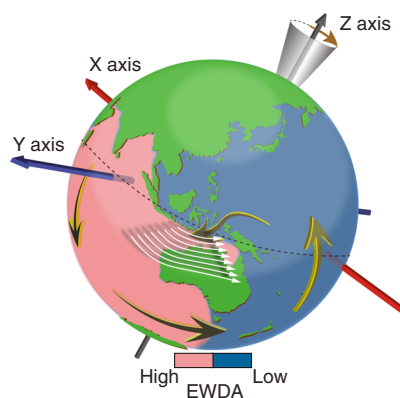


Fig. 5 Schematic diagram of Indo-Pacific see-saw-induced polar motion.

Schematic illustration of a positive cycle of the see-saw in the oceanic mass in the Indo-Pacific basin due to boreal winter MJO winds over the Maritime Continent and its subsequent manifestation in the wobbling of the Earth at intraseasonal timescales. The green color represents landmasses. The color bar signifies intraseasonal equivalent water depth anomaly. The white color arrows over the Maritime Continent depict zonal wind patterns due to MJO. The increasing southward arrow length of the wind vector signifies a negative vertical component of the wind stress curl and consequently a positive source term for barotropic dynamics. The anticlockwise barotropic circulation around the Australian continent is denoted by the curly yellow arrows. The three axes of the solid Earth are represented by the red (x-axis), blue (y-axis), and black (z-axis) arrows. The wobbling of the z-axis is represented by the brown arrow. The black dashed line represents the Equator. The wind and the circulation reverse direction during the negative cycle of the see-saw.

demonstrates that the wind stress over the small region of the Maritime Continent is indeed able to cast a significant influence on the polar motion of the solid Earth during the boreal winter of 2012–2013.

Summary. The MJO winds, acting over ~4% of the Earth’s surface, induce a global-scale ocean mass redistribution, which in turn significantly influences the Earth rotation. This entire phenomenon is schematically illustrated in Fig. 5. The strong boreal winter MJO winds over the Maritime Continent elicit an intraseasonal large-scale barotropic response from the Indian and the Pacific Ocean whose extent is not only limited to the tropics but

also reaches the extratropics within a span of days compared to earlier estimates of months deduced from slow-moving baroclinic excitations. The winds induce a barotropic circulation around the Australian continent and its periodic reversal at intraseasonal timescales is manifested as a see-saw in the oceanic mass within the Indo-Pacific basin. The large-scale oceanic mass redistribution in the Indo-Pacific basin, accompanied by large-scale to-and-fro transports in the two basins associated with this see-saw, benefits from a favorable geometry to excite polar motions. The strong 2013 MJO allowed us to detect the signature of a mode of variability on the polar motion through the ocean. The large oceanic excitation is comparable in magnitude, but out of phase, with the atmospheric excitation and stabilizes the large polar motion changes induced by the atmosphere to the solid Earth.

The magnitude of the see-saw reported here implies that the intraseasonal barotropic variability of the ocean needs to be carefully considered while interpreting the mass budget of the various ocean basins. As the MJOs are intensifying and getting erratic with each passing year^{28,29}, detectable MJO signatures in the polar motion are expected to be more frequent in coming years.

Methods

Model. The state-of-the-art ocean/sea-ice general circulation model (OGCM)—Nucleus for European Modeling of the Ocean (NEMO-version 3.6 stable)¹⁶ is used in this study. The ocean component of NEMO is based on version 9.1 of the OPA primitive equation z -level model with hydrostatic and Boussinesq approximations^{30,31}. This OGCM is coupled to the Louvain-la-Neuve (LIM3) sea ice model³². All simulations analyzed in this study are performed using the NEMO-based eddy-resolving model configuration (ORCA12) developed under the Copernicus Marine Environment Monitoring Service (CMEMS) framework³³.

The NEMO-ORCA12 is a global ocean configuration with an orthogonal, curvilinear, tripolar Arakawa C-type grid with a nominal resolution of $1/12^\circ$ ³⁴. In the tripolar ORCA12 grid, the horizontal resolution gets finer with increasing latitude, i.e., 9 km at the equator, 7 km at mid-latitudes, and 2 km near the poles³⁵. Our model set-up consists of 75 vertical levels and a partial cell representation of bottom topography^{36,37}. The resolution of this vertical discretization decreases from 1 m at the surface to 200 m in the deep ocean. The NEMO-ORCA12 configuration uses a nonlinear free surface with a split-explicit formulation to compute barotropic and baroclinic modes³⁸ and a z^* coordinate approach³⁹. In the z^* formulation, the variation of the column thickness due to sea surface undulations is not concentrated in the surface level, as in the z -coordinate formulation, but is equally distributed over the full water column. Any freshwater flux is considered as a supplementary mass and therefore modifies the volume. A baroclinic time step of 360 s and a barotropic time step of 12 s are used. The momentum advection scheme is a 3rd order Upstream-Biased Scheme⁴⁰ that contains a biharmonic-like dissipation term. A total variance diminishing advection scheme is used for the tracers^{41,42}, and the mixing scheme is k - ϵ ⁴³ based on the Generic Length Scale (GLS) turbulent closure scheme^{44,45}.

The model requires the following fluxes—wind, radiative fluxes, air temperature, rain, and specific humidity. There is no atmospheric pressure gradient forcing in the model as the effect of atmospheric pressure on open-ocean bottom pressure is negligible at timescales longer than ~ 3 days⁴⁶. Snow and river runoff fluxes are monthly climatological forcings obtained from climatology⁴⁷, ETOPO1⁴⁸ and GEBCO_08⁴⁹ have been combined to derive ORCA12 bathymetry³⁶. The minimum depth in the model is set to 12 m. Regions shallower than 12 m are deepened to the minimum depth. The above configuration is the same across the control run and the two sensitivity experiments. Ocean bottom pressure (in decibars) is computed within the model. We obtain intraseasonal equivalent water depth from the model-derived ocean bottom pressure by scaling it with density and applying a Lanczos filter⁵⁰.

Control run. The global NEMO is run for the period 2009–2019 starting from an initial condition obtained from a 30-year spin-up of the model using ERA-Interim ECMWF reanalysis⁵¹. Subsequently, the model is forced with six-hourly National Centre for Medium Range Weather Forecasting (NCMRWF) fluxes⁵² from January 2009 and is run till August 2019. Sea surface temperature (SST) and sea surface salinity (SSS) are weakly restored to the monthly climatological values derived from World Ocean Atlas 2013 (WOA13)^{53,54}. The restoration timescale is 2 months.

Sensitivity experiment: MC-EXP. To understand the importance of MJO winds over the Maritime Continent in establishing the see-saw in the Indo-Pacific oceanic mass, a sensitivity experiment (MC-EXP) is carried out by restricting the wind forcing to the boxed region (90° – 140° E, 32° S– 2° N, black box) in Fig. 2b and zero elsewhere. All other fluxes are prescribed across the globe. The wind mask

is created using a hyperbolic tangent function. To avoid numerical instabilities, the winds at the edges of the box are smoothly decayed to zero over a length scale of 300 km.

The 6-hourly NCMRWF⁵² forcing is used for the wind while the rest of the fluxes are climatological and taken from CORE-II climatology fluxes⁵⁵. The simulation is performed for the period 2009–2019 starting from the same initial condition as the control run. In this experiment, SST and SSS are restored strongly (timescale of 12 h) to the climatological values derived from World Ocean Atlas 2013 (WOA13)^{53,54}. This is done to keep the baroclinic structure of the ocean close to reality in the absence of wind fluxes outside the Maritime Continent.

Bottom pressure recorder data processing. The bottom pressure recorder measures ocean bottom pressure in pounds per square inch absolute (PSIA). This information is disseminated as equivalent water depth after applying a constant 670.0 mm of water/PSIA conversion factor. The bottom pressure recorders have a time resolution of 15 min when operating in the normal mode. However, we chose hourly data by subsampling only the zeroth minute of every hour from the normal mode data. The hourly data are subjected to TASK2000⁵⁶ software to remove tidal frequencies. For this study, a total of 82 bottom pressure recorders were processed. All the bottom pressure recorders were processed using the method described in ref. 4 and a continuous de-tided daily time series was constructed. Intraseasonal equivalent water depth was estimated from the daily time series using the Lanczos filter⁵⁰.

Estimation of degree of freedom for a band-passed time series. The formula for estimating the degree of freedom (DOF) for a band-passed time series⁵⁷ is

$$DOF = 2N \left(\frac{\Delta T}{T_{c1}} - \frac{\Delta T}{T_{c2}} \right) - 2, \quad (1)$$

where ΔT is the sample interval, T_{c1} and T_{c2} are the cutoff periods in the band-pass filtering ($T_{c1} < T_{c2}$) and N is the sample size. In this study for intraseasonal (30–80 days) band-pass filter, ΔT is taken as 1 day, T_{c1} and T_{c2} are 30 and 80 days, respectively, and N is 1501 (10 years of daily data during December–April). Based on this equation, we estimated that the DOF for the winter months (December–April) of 2009–2019 is 60. Corresponding to this DOF, the correlation values greater than 0.21 and less than -0.21 are 90% significant in accordance with the Pearson correlation table.

Estimation of ocean excitation functions from the model. Changes in the polar motion of the solid earth due to the ocean can be attributed to the changes in ocean mass distribution and/or changes in ocean currents⁵⁸. Daily excitations in the polar motion due to oceanic mass and currents are computed from our model using the algorithm adapted from ref. 8. The polar motion excitation functions χ_1 and χ_2 describe the effective changes in the angular momentum components about two equatorial axes are conventionally taken to point toward the Greenwich (x axis) and 90° E meridians (y axis), respectively. These two excitation functions, χ_1 and χ_2 , can be expressed as the sum of a mass term and a motion term (Eq. (2)),

$$\begin{bmatrix} \chi_1 \\ \chi_2 \end{bmatrix} = \begin{bmatrix} \chi_1^{\text{mass}} \\ \chi_2^{\text{mass}} \end{bmatrix} + \begin{bmatrix} \chi_1^{\text{motion}} \\ \chi_2^{\text{motion}} \end{bmatrix} \quad (2)$$

$$\begin{bmatrix} \chi_1^{\text{mass}} \\ \chi_2^{\text{mass}} \end{bmatrix} = - \frac{1.44R^2}{1.61(C-A)} \int_V \left(\rho \sin \theta \cos \theta \begin{bmatrix} \cos \lambda \\ \sin \lambda \end{bmatrix} \right) dV \quad (3)$$

$$\begin{bmatrix} \chi_1^{\text{motion}} \\ \chi_2^{\text{motion}} \end{bmatrix} = \frac{1.61R}{\Omega(C-A)} \int_V \rho \left(u \begin{bmatrix} -\sin \theta \cos \lambda \\ -\sin \theta \sin \lambda \end{bmatrix} + v \begin{bmatrix} \sin \lambda \\ -\cos \lambda \end{bmatrix} \right) dV \quad (4)$$

From the model, the changes in the excitation function due to the oceanic mass redistribution (Eq. (3)) were computed by integrating the density (ρ) over the ocean volume (V). Similarly, changes due to the currents (Eq. (4)) were computed by integrating density (ρ) multiplied by the zonal (u) and meridional (v) currents over the ocean volume. The partial cell representation of bottom topography in the model was accounted for during the vertical integration along with the depth of the ocean. In Eqs. (3) and (4), R (6371 km) and Ω ($7.2921 \times 10^{-5} \text{ s}^{-1}$) are the Earth's mean radius and angular velocity, respectively, A ($7.0161 \times 10^{37} \text{ kg m}^2$) and C ($7.041 \times 10^{37} \text{ kg m}^2$) are the equatorial and polar moments of inertia of the solid Earth. λ and θ represent the longitude and the latitude. The factor of 1.44 accounts for the yielding of the solid Earth to imposed surface loads, and the factor of 1.61 includes the effect of core decoupling. Intraseasonal χ_1 and χ_2 were obtained from the daily χ_1 and χ_2 using Lanczos filter⁵⁰.

Data availability

Bottom pressure recorder data were downloaded from NDBC (<http://www.ndbc.noaa.gov/dart.shtml>), INCOIS/NIOT (<https://www.incois.gov.in>), ROSAME (<http://www.legos.obs-mip.fr/observations/rosame>), SAMOC (https://www.aoml.noaa.gov/phod/SAMOC_inter-national), ABPR (<http://psc.apl.washington.edu/northpole/Data.html>), and BGEP (<https://www.whoi.edu/page.do?pid=66559>). Bottom pressure recorder data located at 37.283° W, 32.2548° N have been obtained in the framework of EMSO-Azores

observatory and the intraseasonal filtered data can be accessed from the link <https://data.mendeley.com/datasets/29h94hnj6k/1>. National Center for Medium Range Weather Forecasting (NCMRWF) fluxes can be obtained on request directed to vsprasad@ncmrwf.gov.in. Real-time Multivariate MJO index (RMM) is available at <http://www.bom.gov.au/bmrc/clfor/cfstaff/matw/maproom/RMM/>. The Earth System Modelling Group of GeoForschungsZentrum Potsdam (ESMGFZ) data is available from <http://rz-vm115.gfz-potsdam.de:8080/repository>. International Earth Rotation and Reference Systems Service (IERS) polar motion excitations are downloaded from <https://hpiers.obspm.fr/eop-pc/analysis/excitative.html>. International Nusantara Stratification And Transport (INSTANT) data are available from <http://www.marine.csiro.au/~cow074/index.htm>.

Received: 8 December 2020; Accepted: 3 June 2021;

Published online: 05 July 2021

References

- Madden, R. A. & Julian, P. R. Detection of a 40–50 day oscillation in the zonal wind in the tropical Pacific. *J. Atmos. Sci.* **28**, 702–708 (1971).
- Madden, R. A. & Julian, P. R. Description of global-scale circulation cells in the tropics with a 40–50 Day Period. *J. Atmos. Sci.* **29**, 1109–1123 (1972).
- Wheeler, M. & Kiladis, G. N. Convectively coupled equatorial waves: analysis of clouds and temperature in the wavenumber–frequency domain. *J. Atmos. Sci.* **56**, 374–399 (1999).
- Rohith, B. et al. Basin-wide sea level coherency in the tropical Indian Ocean driven by Madden–Julian Oscillation. *Nat. Commun.* **10**, 1257 (2019).
- Ponte, R. M. & Gutzler, D. S. The Madden-Julian oscillation and the angular momentum balance in a barotropic ocean model. *J. Geophys. Res. Ocean.* **96**, 835–842 (1991).
- Zhang, C. Madden-Julian Oscillation. *Rev. Geophys.* **43**, RG2003 (2005).
- Oliver, E. C. J. & Thompson, K. R. Madden-Julian Oscillation and sea level: local and remote forcing. *J. Geophys. Res.* **115**, C01003 (2010).
- Gross, R. S., Fukumori, I. & Menemenlis, D. Atmospheric and oceanic excitation of the Earth's wobbles during 1980–2000. *J. Geophys. Res.* **108**, 2370 (2003).
- Gross, R. S., Fukumori, I., Menemenlis, D. & Gegout, P. Atmospheric and oceanic excitation of length-of-day variations during 1980–2000. *J. Geophys. Res. Solid Earth* **109**, B01406 (2004).
- Ponte, R. M., Stammer, D. & Marshall, J. Oceanic signals in observed motions of the Earth's pole of rotation. *Nature* **391**, 476–479 (1998).
- Lambeck, K. *The Earth's variable rotation* (Cambridge University Press 1980).
- Gross, R. S. in *Treatise on Geophysics* (ed. Herring, T. A.) Vol. 11, 239–294 (Elsevier, 2007).
- Barnes, R. T. H., Hide, R., White, A. A. & Wilson, C. A. Atmospheric angular momentum fluctuations, length-of-day changes and polar motion. *Proc. R. Soc. London. A.* **387**, 31–73 (1983).
- Gross, R. S., Chao, B. F. & Desai, S. D. Effect of long-period ocean tides on the Earth's polar motion. *Prog. Oceanogr.* **40**, 385–397 (1997).
- Nastula, J. & Ponte, R. M. Further evidence for oceanic excitation of polar motion. *Geophys. J. Int.* **139**, 123–130 (1999).
- Zhou, Y. H., Chen, J. L., Liao, X. H. & Wilson, C. R. Oceanic excitations on polar motion: a cross comparison among models. *Geophys. J. Int.* **162**, 390–398 (2005).
- Madec, G. & the NEMO Team. NEMO ocean engine - version 3.6. *Note du Pôle modélisation*, Inst. Pierre-Simon Laplace, No. 27 (2014).
- Cheng, X., Li, L., Du, Y., Wang, J. & Huang, R. -X. Mass-induced sea level change in the northwestern North Pacific and its contribution to total sea level change. *Geophys. Res. Lett.* **40**, 3975–3980 (2013).
- Fukumori, I., Wang, O., Llovel, W., Fenty, I. & Forget, G. A near-uniform fluctuation of ocean bottom pressure and sea level across the deep ocean basins of the Arctic Ocean and the Nordic Seas. *Prog. Oceanogr.* **134**, 152–172 (2015).
- McCreary, J. P. et al. Interactions between the Indonesian throughflow and circulations in the Indian and Pacific Oceans. *Prog. Oceanogr.* **75**, 70–114 (2007).
- Chandler, S. C. On the variation of latitude. *I. Astron. J.* **11**, 59–61 (1981).
- Gross, R. S. The excitation of the Chandler wobble. *Geophys. Res. Lett.* **27**, 2329–2332 (2000).
- Dill, R., Dobslaw, H. & Thomas, M. Improved 90-day Earth orientation predictions from angular momentum forecasts of atmosphere, ocean, and terrestrial hydrosphere. *J. Geod.* **93**, 287–295 (2019).
- Dobslaw, H., Dill, R., Grötzsch, A., Brzeziński, A. & Thomas, M. Seasonal polar motion excitation from numerical models of atmosphere, ocean, and continental hydrosphere. *J. Geophys. Res.* **115**, B10406 (2010).
- Dobslaw, H. & Dill, R. Predicting earth orientation changes from global forecasts of atmosphere-hydrosphere dynamics. *Adv. Sp. Res.* **61**, 1047–1054 (2018).
- Yu, N., Li, J., Ray, J. & Chen, W. Improved geophysical excitation of length-of-day constrained by earth orientation parameters and satellite gravimetry products. *Geophys. J. Int.* **214**, 1633–1651 (2018).
- Luo, J., Chen, W., Ray, J. & Li, J. Excitations of length-of-day seasonal variations: analyses of harmonic and inharmonic fluctuations. *Geod. Geodyn.* **11**, 64–71 (2020).
- Arnold, N. P., Branson, M., Kuang, Z., Randall, D. A. & Tziperman, E. MJO intensification with warming in the superparameterized CESM. *J. Clim.* **28**, 2706–2724 (2015).
- Haertel, P. Prospects for erratic and intensifying Madden-Julian oscillations. *Climate* **8**, 24 (2020).
- Marzocchi, A. et al. The North Atlantic subpolar circulation in an eddy-resolving global ocean model. *J. Mar. Syst.* **142**, 126–143 (2015).
- Smith, G. C. et al. Impact of coupling with an ice-ocean model on global medium-range NWP forecast skill. *Mon. Weather Rev.* **146**, 1157–1180 (2018).
- Rousset, C. et al. The Louvain-La-Neuve sea ice model LIM3.6: global and regional capabilities. *Geosci. Model Dev.* **8**, 2991–3005 (2015).
- Lellouche, J.-M. et al. Recent updates to the Copernicus Marine Service global ocean monitoring and forecasting real-time 1/2° high-resolution system. *Ocean Sci.* **14**, 1093–1126 (2018).
- Rieck, J. K., Böning, C. W., Greatbatch, R. J. & Scheinert, M. Seasonal variability of eddy kinetic energy in a global high-resolution ocean model. *Geophys. Res. Lett.* **42**, 9379–9386 (2015).
- Gasparin, F. et al. A large-scale view of oceanic variability from 2007 to 2015 in the global high resolution monitoring and forecasting system at Mercator Océan. *J. Mar. Syst.* **187**, 260–276 (2018).
- Adcroft, A., Hill, C. & Marshall, J. Representation of topography by shaved cells in a height coordinate ocean model. *Mon. Weather Rev.* **125**, 2293–2315 (1997).
- Bernard, B. et al. Impact of partial steps and momentum advection schemes in a global ocean circulation model at eddy-permitting resolution. *Ocean Dyn.* **56**, 543–567 (2006).
- Shchepetkin, A. F. & McWilliams, J. C. The regional oceanic modeling system (ROMS): a split-explicit, free-surface, topography-following-coordinate oceanic model. *Ocean Model.* **9**, 347–404 (2005).
- Adcroft, A. & Campin, J.-M. Rescaled height coordinates for accurate representation of free-surface flows in ocean circulation models. *Ocean Model.* **7**, 269–284 (2004).
- Shchepetkin, A. F. & McWilliams, J. C. in *Computational Methods for the Ocean and the Atmosphere*. (ed. Ciarlet, P. G.) Vol. 14, 121–183 (Elsevier Science 2008).
- Cravatte, S., Madec, G., Izumo, T., Menkes, C. & Bozec, A. Progress in the 3-D circulation of the eastern equatorial Pacific in a climate ocean model. *Ocean Model.* **17**, 28–48 (2007).
- Lévy, M., Estublier, A. & Madec, G. Choice of an advection scheme for biogeochemical models. *Geophys. Res. Lett.* **28**, 3725–3728 (2001).
- Rodi, W. Examples of calculation methods for flow and mixing in stratified fluids. *J. Geophys. Res.* **92**, 5305 (1987).
- Umlauf, L. & Burchard, H. A generic length-scale equation for geophysical turbulence models. *J. Mar. Res.* **61**, 235–265 (2003).
- Reffray, G., Bourdalle-Badie, R. & Calone, C. Modelling turbulent vertical mixing sensitivity using a 1-D version of NEMO. *Geosci. Model Dev.* **8**, 69–86 (2015).
- Ponte, R. M. Understanding the relation between wind- and pressure-driven sea level variability. *J. Geophys. Res.* **99**, 8033 (1994).
- Dai, A., Qian, T., Trenberth, K. E. & Milliman, J. D. Changes in continental freshwater discharge from 1948 to 2004. *J. Clim.* **22**, 2773–2792 (2009).
- Amante, C. & Eakins, B. W. ETOPO1 1 arc-minute global relief model: procedures, data sources and analysis. NOAA Technical Memorandum NESDIS NGDC-24. *Vasa.* **19**, 1–25 (2009).
- Becker, J. J. et al. Global bathymetry and elevation data at 30 arc seconds resolution: SRTM30_PLUS. *Mar. Geod.* **32**, 355–371 (2009).
- Duchon, C. E. Lanczos filtering in one and two dimensions. *J. Appl. Meteorol.* **18**, 1016–1022 (1979).
- Dee, D. P. et al. The ERA-Interim reanalysis: configuration and performance of the data assimilation system. *Q. J. R. Meteorol. Soc.* **137**, 553–597 (2011).
- Prasad, V. S. et al. Improvements in medium range weather forecasting system of India. *J. Earth Syst. Sci.* **123**, 247–258 (2014).
- Locarnini, R. A. et al. S. Levitus, Ed.; A. Mishonov, Technical Ed, World Ocean Atlas 2013 Volume 1: Temperature. NOAA Atlas NESDIS **73**, 40 (2013).
- Zweng, M. M. et al. S. Levitus, Ed.; A. Mishonov, Technical Ed, World Ocean Atlas 2013, Volume 2: Salinity. NOAA Atlas NESDIS. **74**, 39 (2013).
- Large, W. G. & Yeager, S. G. The global climatology of an interannually varying air-sea flux data set. *Clim. Dyn.* **33**, 341–364 (2009).
- Murray, M. T. A general method for the analysis of hourly heights of the tide. *Int. Hydrogr. Rev.* **41**, 91–101 (1964).

57. Bendat, J. S. & Piersol, A. G. *Random Data: Analysis and Measurement Procedures* 4th edn, (John Wiley & Sons, Inc., 2010).
58. Chen, J.-L., Wilson, C. R., Hu, X.-G., Zhou, Y.-H. & Tapley, B. D. Oceanic effects on polar motion determined from an ocean model and satellite altimetry: 1993-2001. *J. Geophys. Res. Solid Earth*. **109**, B02411 (2004).
59. Wheeler, M. C. & Hendon, H. H. An all-season real-time multivariate MJO index: development of an index for monitoring and prediction. *Mon. Weather Rev.* **132**, 1917–1932 (2004).

Acknowledgements

M.A is grateful to Mercator Ocean International for the academic visit. We are grateful to INCOIS and the Ministry of Earth Sciences (MoES) for providing facilities. This work is supported by INCOIS, MOES, and by the project “Barotropic Influence on Global Ocean (BINGO); grant no 41-DS-GMMC-BINGO-CNRS195918”. M.A., B.R., and A.P. are grateful to Balaji Baduru for useful discussions on statistical analysis. The lead author is grateful to the Council of Scientific and Industrial Research (CSIR) for providing a Research Fellowship grant. This is INCOIS contribution number 423.

Author contributions

A.P., F.D., B.R., and S.S.C.S. conceived the idea. M.A. carried out the NEMO runs aided by B.R., R.B.B., and F.D. P.V.S. had carried out similar model experiments, supported by M.A. and B.R., using coarser MOM5.0 in her project dissertation with A.P. B.R. processed the bottom pressure recorder data. A.P., F.D., B.R., M.A., and R.B.B. analyzed the results. A.P., F.D., and O.d.V. wrote the manuscript and others corrected it. V.B. provided bottom pressure data located at 37.283°W, 32.2548°N. All authors contributed to the material of the paper through multiple discussions.

Competing interests

The authors declare no competing interests.

Additional information

Supplementary information The online version contains supplementary material available at <https://doi.org/10.1038/s43247-021-00210-x>.

Correspondence and requests for materials should be addressed to A.P.

Peer review information *Communications Earth & Environment* thanks the anonymous reviewers for their contribution to the peer review of this work. Primary Handling Editors: Joy Mervin Monteiro, Heike Langenberg. Peer reviewer reports are available.

Reprints and permission information is available at <http://www.nature.com/reprints>

Publisher's note Springer Nature remains neutral with regard to jurisdictional claims in published maps and institutional affiliations.



Open Access This article is licensed under a Creative Commons Attribution 4.0 International License, which permits use, sharing, adaptation, distribution and reproduction in any medium or format, as long as you give appropriate credit to the original author(s) and the source, provide a link to the Creative Commons license, and indicate if changes were made. The images or other third party material in this article are included in the article's Creative Commons license, unless indicated otherwise in a credit line to the material. If material is not included in the article's Creative Commons license and your intended use is not permitted by statutory regulation or exceeds the permitted use, you will need to obtain permission directly from the copyright holder. To view a copy of this license, visit <http://creativecommons.org/licenses/by/4.0/>.

© The Author(s) 2021